Faculteit Wetenschappen
Vakgroep Fysica en Sterrenkunde

Academiejaar 2011–2012

Ab initio prediction of material properties for the inner core of the planet Mercury

Jan Jaeken

Promotoren
Prof. Dr. M. Waroquier
Prof. Dr. S. Cottenier

Scriptie ingediend tot het behalen van de academische graad van
Master in de Fysica en Sterrenkunde

Voorwoord

Mijn Masterthesis, een mijlpaal in mijn studieloopbaan. Het einde van iets, en het begin van veel meer. Het is onvoorstelbaar hoe veel een mens kan bijleren op enkele jaren tijd, en hoe overweldigend veel er nog te leren valt. Met het indienen en verdedigen van dit werk, hoop ik mij trots "Master in de Wetenschappen" te kunnen noemen. Maar deze titel behalen en deze thesis schrijven had ik nooit alleen gekund. Daarom zijn er enkele mensen die ik wil bedanken, omdat zonder hen dit werk niet zou zijn geworden wat het is.

Eerst en vooral wil ik Stefaan Cottenier bedanken om mij te begeleiden tijdens de voorbije maanden. Zijn heldere uitleg en constante feedback zijn onontbeerlijk geweest om deze thesis in goede banen te leiden. Ook wil ik hem samen met Michel Waroquier bedanken om mij de kans te geven deze Masterthesis te doen.

Kurt Lejaeghere was een constante hulplijn bij de praktische computationele kant van deze thesis, en Tim Van Hoolst van de Koninklijke Sterrenwacht in Brussel heeft meegeholpen deze thesis op poten te zetten met zijn planetologische expertise.

Ik wil ook een oprecht dankwoord richten aan mijn ouders, om mij al die jaren onaflatend te steunen in mijn studies, en mij vrij te laten in mijn studiekeuzes. Dat was een belofte die jullie jaren geleden hebben gedaan en nooit hebben verbroken.

Als laatste, maar zeker niet in het minst, wil ik Iris bedanken. Zonder jouw steun en aanwezigheid, zowel tijdens woelige thesistijden als daarbuiten, was ik niet geraakt waar ik nu ben. Samen kunnen we de wereld aan.

Jan Jaeken
Gent, januari 2012

Samenvatting

In dit werk wordt onderzocht in welke mate en op welke manier *ab initio* methodes, meer bepaald dichtheidsfunctionaaltheorie, de materiaaleigenschappen kunnen voorspellen van niet-magnetisch vlakgecentreerd kubisch ijzer zoals het voorkomt in de kern van Mercurius. Planeet Mercurius heeft de hoogste massadichtheid van alle rotsplaneten (na het corrigeren voor zelfcompressie). Dit impliceert dat er een grote hoeveelheid ijzer aanwezig is, zodat de kern van de planeet een straal heeft van wel 70% de straal van Mercurius zelf. Er zijn nog veel open vragen omtrent Mercurius, zoals hoe zijn magneetveld wordt opgewekt, wat de precieze samenstelling is van de kern, en hoe veel van de kern vloeibaar is. Omdat het moeilijk is rechtstreekse informatie hierover te verkrijgen, kunnen ab initio methoden bijdragen aan de kennis van de kern van deze planeet. Het is bijvoorbeeld nog onduidelijk hoe veel zwavel er voorkomt in de Mercuriuskern. Informatie over de effecten die zwavelonzuiverheden hebben op ijzer onder hoge druk en temperatuur kunnen dus helpen om planetologische modellen te verfijnen.

Er wordt algemeen aangenomen dat het ijzer in de kern van Mercurius zich bevindt in de vlakgecentreerd kubische (fcc) fase. Daarom handelt deze thesis ook over de materiaaleigenschappen van fcc ijzer bij hoge druk (ongeveer 0 GPa tot 70 GPa) en hoge temperatuur (ongeveer 1000 K tot 3000 K). In dit geïdealiseerd model zijn er geen onzuiverheden aanwezig en spelen magnetische effecten geen rol.

De roosterparameter van fcc ijzer, en dus ook de dichtheid van het materiaal, kunnen bepaald worden bij 0 K en 0 GPa door rechtstreekse toepassing van methoden die op dichtheidsfunctionaaltheorie zijn gebaseerd.

Om thermische effecten in rekening te brengen, worden de eigenschappen van harmonische roostertrillingen (fononen) bepaald. Dit wordt gedaan door middel van krachtberekeningen met dichtheidsfunctionaaltheorie. Door de terugroepende kracht op een verplaatst atoom, en de resulterende krachten op andere atomen te bepalen, kunnen dispersierelaties van fononen bepaald worden. Hiermee wordt dan, op statistisch mechanische wijze, de Helmholtz vrije energie $F(T)$ in functie van de temperatuur berekend. Hieruit volgt ook de entropische bijdrage van de roostertrillingen $S(T)$ en de warmtecapaciteit van het materiaal $C_V(T)$. Om het effect van druk te bepalen wordt de zgn. quasi-harmonische benadering gebruikt, waarbij voor verschillende waarden van de roosterparameter de (harmonische) fononeneigenschappen worden bepaald. Door deze volumeveranderingen veranderen ook

de fononeneigenschappen, wat vervolgens weer een effect heeft op de entropie en de vrije energie.

Door bovenstaande te combineren kan de Gibbs vrije energie $G(p, T)$ worden bepaald in functie van druk en temperatuur. Hieruit volgt het evenwichtsvolume (dus ook de roosterparameter en de dichtheid) in functie van druk en temperatuur. Door de volumeverandering in functie van temperatuur te beschouwen, kan dan ook de thermische expansie $\alpha(p, T)$ worden afgeleid.

Om de computationele berekeningen zo betrouwbaar mogelijk te maken, zijn uitgebreide convergentietesten gebeurd op alle relevante, instelbare parameters. De uiteindelijke resultaten zijn vergeleken met beschikbare experimentele data, waarbij werd gekeken naar volume en thermische expansie. Hieruit bleek dat het volume meer dan gebruikelijk werd onderschat, terwijl de thermische expansie vrij getrouw werd gereproduceerd.

De resultaten van deze thesis geven een opstap naar een waaier van toepassingen van ab initio methodes in de context van planetaire kernen. Naast de massadichtheid kan ook worden gekeken naar elastische eigenschappen zoals de compressiemodulus, de schuifmodulus of de elasticiteitsmodulus. Verder kan worden bestudeerd welke effecten er optreden bij het toevoegen van onzuiverheden in verschillende concentraties, zoals zwavel.

Contents

Chapter 1

Introduction

Mercury, as shown in fig. 1.1, is the smallest and innermost planet of the solar system. It still holds many mysteries, partly because it's fairly difficult to observe. Due to its close proximity to the Sun, Mercury is never seen further than 27.8° from the Solar glare in the sky. For precisely this reason, it is forbidden to use the Hubble Space Telescope to observe Mercury, as accidentally pointing it directly at the Sun may damage the sensitive equipment. Spacecraft missions have been scarce, since orbits around Mercury tend to be unstable, again due to its close proximity to the Sun, combined with its fairly high orbital eccentricity of 0.2056 [1].

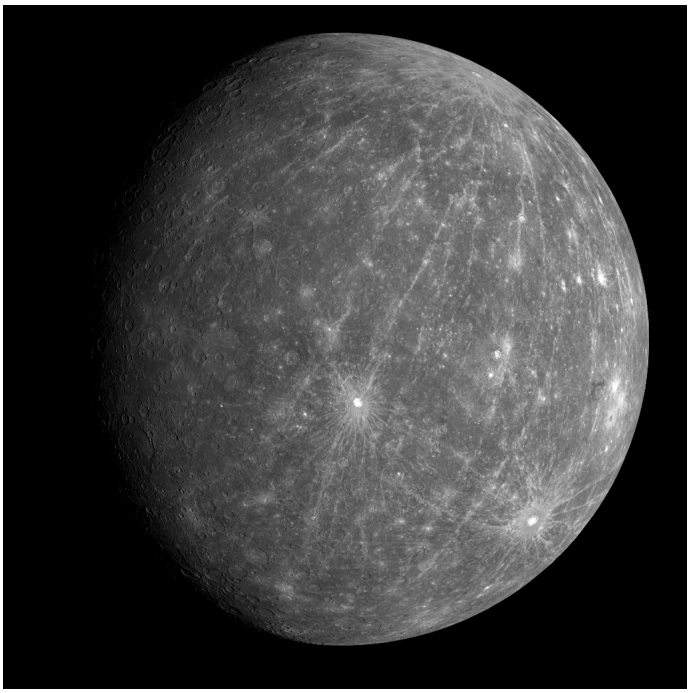

Figure 1.1: Mercury as imaged by the MESSENGER spacecraft during its second flyby on Jan 6th, 2008. Credit: NASA/Johns Hopkins University Applied Physics Laboratory/Carnegie Institution of Washington.

Before 2008, much of what was known about Mercury dated from information gathered during three flybys done by the Mariner 10 spacecraft in 1974-1975, imaging 45% of its surface [2]. It remained the only spacecraft to travel near Mercury until the American MESSENGER probe made its first flyby in January of 2008. Another space mission, BepiColombo [3] is planned by a collaboration between the European (ESA) and Japanese (JAXA) space agencies and is scheduled to be launched in 2014. The complementing designs of the MESSENGER and BepiColombo missions show promise to answer many questions about Mercury, as well as to raise many new ones. MESSENGER is currently in orbit around Mercury, gathering much information about its surface, exosphere, magnetic field and gravitational field. The BepiColombo mission consists of two spacecraft: The Mercury Planetary Orbiter (MPO), to accurately measure spectroscopic data of the surface; and the Mercury Magnetospheric Orbiter (MMO), designed to study Mercury's magnetic field in great detail.

Mercury is the densest terrestrial planet (after correcting for self-compression) [4] to circle the Sun. Its mean density of 5423 kg m^{-3}, together with standard planetary formation models and nuclear abundance, implies a very high iron content. So high, in fact, that its core has a radius of at least 70% that of the planet itself [5]. The current understanding of the interior structure of Mercury is shown in fig. 1.2, in which it is clear that most of the planet consists of the ferric core, with a fairly small silicate mantle above, topped off by the crust. The planet also has an intrinsic dipolar magnetic field, which is probably generated by a geothermal dynamo [6]. Earth-based radar measurements have determined that Mercury's core is at least partially molten [7], making the existence of such a dynamo even more likely. On the other hand, the driving force behind such a system is the solidification of an inner core, meaning that Mercury's core is almost certainly part liquid, part solid.

One of the great open questions concerning Mercury is the structure, composition and state of its core. Much can be inferred from spacecraft missions and planetological formation models, yet there is of course no practically conceivable way of directly confirming such models. One modern possibility is using a computational *ab initio* approach. Starting from an initial composition, initial crystal structure and the laws of quantum physics and statistical mechanics, it is possible to predict material properties at arbitrary pressure and temperature. It is then possible to compare these values with those acquired from planetological models and planetary observations. Computational methods are an interesting way to add to the available information about planetary cores, especially at pressure and temperature regimes where experimental information is sparse or even unobtainable.

This thesis is about computationaly predicting the properties of non-magnetic face-centered cubic (fcc) iron (see fig. 1.3), as it is believed to be the dominant constituent of the core of planet Mercury (see fig. 1.5 [5] and fig. 1.4 [4]). The core of the planet Mercury (as those of the other terrestrial planets) consists of an iron-nickle alloy (up to 8%wt. Ni) with an uncertain (1%wt. to 6%wt.) amount of sulfur [7][8]. As can be seen on the phase diagram

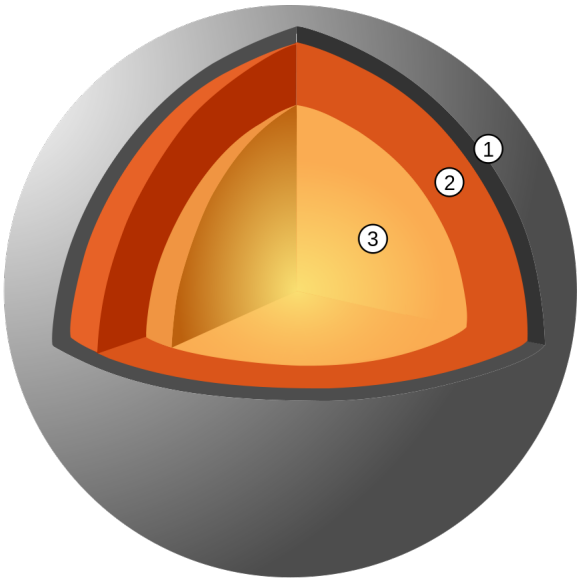

Figure 1.2: Diagram of the internal structure of the planet Mercury. (1) Crust, 100-200 km thick; (2) Mantle, 600 km thick; (3) Core, 1800 km radius. Image by Joel Holdsworth.

in fig. 1.5, solid iron at a pressure between 7 and 39 GPa [4] and a temperature between 2000 and 2500 K [8] is in the fcc phase.

This form of iron seems to have a Curie temperature of around 500 K [9] when grown in atomic layers upon Cu, and the relevant temperature ranges for this work are even above the 1043 K Curie temperature of bcc iron. Applying pressure increases the overlap between atomic orbitals and this reduces magnetic effects, which can be experimentally observed as a reduced magnetization and a reduced Curie temperature. The pressure in the inner core of Mercury is quite high compared to pressures routinely applied to solids. Therefore, by the combined effect of temperature and pressure, it is reasonable to assume the solid iron at Mercury inner core conditions to be nonmagnetic. From here on, it is assumed there are no magnetic effects and no impurities, meaning that only the properties of pure non-magnetic fcc Fe are considered.

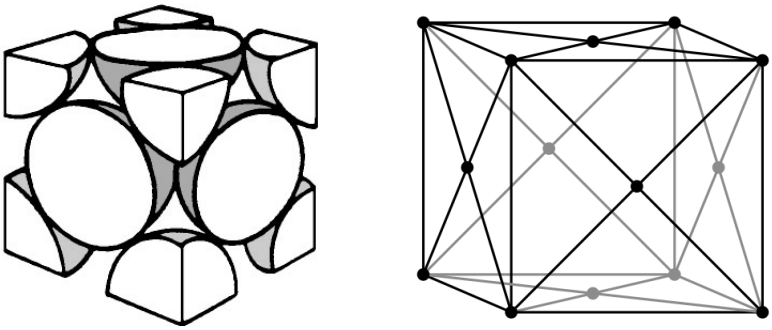

Figure 1.3: The face-centered cubic (fcc) crystal structure.

The fundamental questions of this work are:

- What are the material properties of non-magnetic fcc Fe at the conditions of the inner core of the planet Mercury?
- How accurate is density functional theory in predicting these properties?

The structure of this text is as follows. Chapter 2 gives a background on the computational methods necessary to do an ab initio prediction of material properties at finite temperature and pressure. Chapter 3 contains a detailed assessment of numerical convergence, which also provides a first estimate of fcc Fe's properties at 0 K and 0 Pa. This is followed by the results of the full quasi-harmonic calculations in chapter 4, with a comparison to experimental data on fcc Fe, as far as it is available. At last, the conclusions can be found in chapter 5, followed by an outlook to future possible applications of computational methods to the open questions concerning Mercury's inner core, and ways to increase the reliability of the current methods.

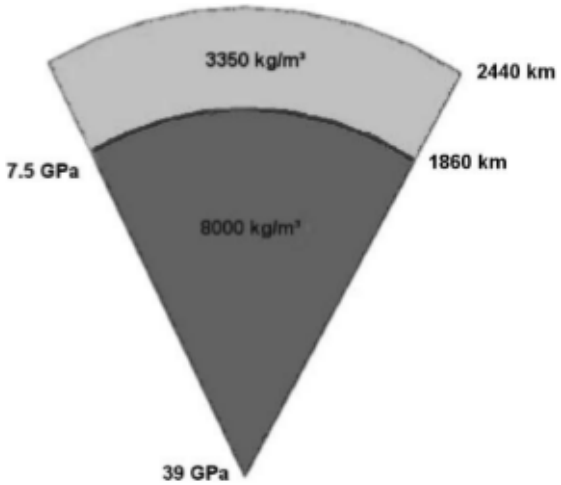

Figure 1.4: Simple approximation of the pressure and density inside planet Mercury. Taken from ref. [4].

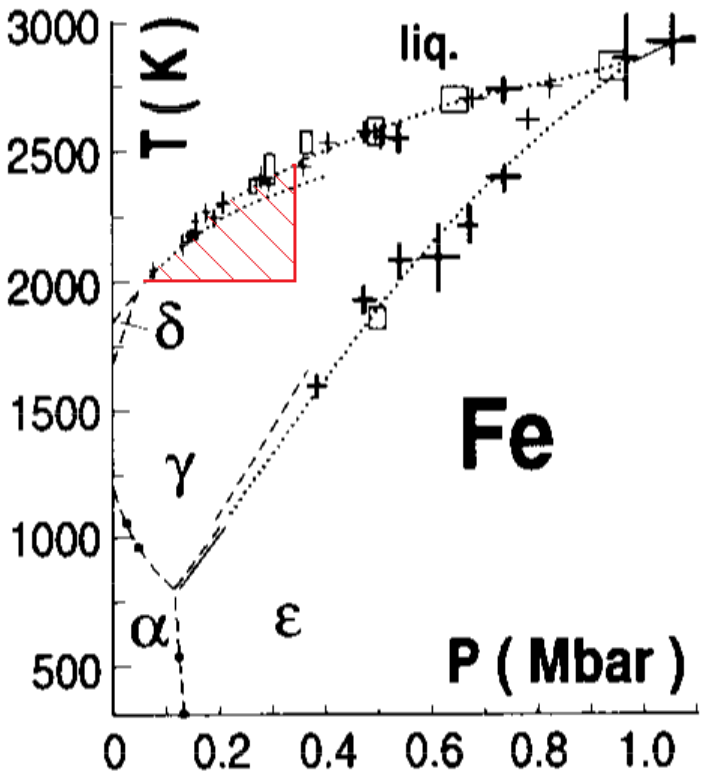

Figure 1.5: Phase diagram of pure iron, adapted from [10]. The phases are labeled as follows: α: bcc, γ: fcc, δ: non-magnetic bcc, ϵ: hcp. The (approximate) conditions present at the inner core of the planet Mercury are shown in red. Only the solid state conditions are marked, as they are the only ones considered in this work. 1 Mbar equals 100 GPa.

Chapter 2

Computational methods

2.1 Density functional theory

This section is meant as a general background on Density functional theory, in which the points most relevant to this work are touched upon. It is not meant to be a thorough explanation, nor a complete summary. Interested readers are refered to the many citations that follow. A clear, general introduction can be found on Wikipedia [11] or in ref. [12]. For a more in-depth treatment, there is ref. [13]. Those who are interested in a more mathematical background can consult, for example, ref. [14].

Density functional theory (DFT) is a successful and widely used theoretical framework for modeling solid and molecular systems. It hinges on the application of the Hohenberg-Khon theorems, which – in the Born-Oppenheimer (clamped-nuclei) approximation – establish the existence of a bijection between the antisymmetric N-body electronic wavefunction and the electronic particle density of the molecular ground state [15]. The existence of this bijection assures that all information contained in the wavefunction is also contained in the ground state density. It follows then that any physical information could, in principle, be obtained from a functional which takes the electronic density as argument. This, however, is far from a trivial task in practice, and much research has gone into finding ways to tease out the appropriate physical information from the particle density, even if only in an approximate way, while still being able to accurately describe physical and chemical systems [12]. One famous approach is to not consider functionals of the density itself, but using a set of fictional non-interacting single-particle wave functions that reproduce the true density. This leads to the Kohn-Sham equations, which have the advantage of having the familiar appearance of a time-independent Schrödinger equation [16].

Furthermore, even after establishing the Kohn-Sham equations, one needs to cast these single-particle wave functions into a managable form, most often expanded in a basis set of simple functions. Again, many basis sets can be and are used in practice, but for solid-state

purposes common choices involve expansions based on plane waves. It is easy to see that a plane wave approach will run into difficulties near nuclei. Therefore, the software used in this work, VASP[17][18][19][20], uses a pre-calculated density in the nuclear neighborhood, based on a pseudopotential approach [21]. This way, only valence electrons are considered in the actual calculation, while the core electrons are frozen in their atomic configuration near the nuclear environment.

Solution schemes in DFT revolve around self consistency, often iterating until some physical parameter (such as the energy) has achieved a desired level of convergence. There is one caveat: the fact that the Hohenberg-Kohn theorems only pertain to the electronic ground state causes DFT to limit its description to systems at a temperature of absolute zero. There is a way around this however, which is described in section 2.3.

2.2 Applying pressure

When performing a solid-state DFT calculation, one starts by specifying the unit cell of the material. This does not need to be the equilibrium structure at 0 Pa. Performing calculations at several values for the primitive unit cell volume V[1] yields the internal energy $U(V)$. To obtain material properties at a pressure of 0 Pa, it is possible to fit an equation of state through these values, hereby obtaining the equilibrium unit cell volume, bulk modulus and derivative of the bulk modulus. This is done elaborately in section 3.1. Further possibilities include calculating the shear modulus or Young's modulus by applying specific deformations of the material structure, and calculating the change in energy U. This was not considered in this work.

To raise the pressure, one can calculate the enthalpy $H = U(V) + pV$ through

$$H(p) = U(V) - \frac{dU(V)}{dV}V = \min_V \left(U(V) + pV\right), \tag{2.1}$$

in which the former is the explicit Legendre transformation, and the latter is the more practical strategy. One determines $U(V)$ for several values of the unit cell volume, and can find $H(p)$ by minimizing $U(V) + pV$, while keeping the pressure p fixed. For a realistic system however, considering pressure is not enough, and one must also take into account temperature effects.

[1]To keep a consistent notation, V is used throughout this work to denote the volume of the primitive cell of the crystal, i.e. the volume of the repeatable unit cell which contains exactly one atom.

2.3 Finite temperature

It is well established [22][23] that nuclear vibrations are the dominant contributor to the thermal properties of a solid, especially for effects such as the volume expansion. For this reason, the focus in this work is on lattice vibrations in order to describe temperature-dependent phenomena. The harmonic approximation to a lattice vibration is commonly called a "phonon". These harmonic contributions constitute by far the largest part of the effects due to lattice vibrations [24]. Thus, for a reliable prediction of material properties at elevated temperatures, calculating the phonon properties is a conceptually clear and reliable strategy. In this work, the software package Phonopy [25] was used to determine phonon properties. Phonopy uses the Parlinski-Li-Kawazoe method [26] of finite-displacement to calculate the phonon dispersion relations, as detailed in section 2.3.1.

2.3.1 The harmonic approximation: phonons

A lucid theoretical background on determining phonon properties can be found in ref. [23]. For the following, it is sufficient to note that the potential energy Φ of a nuclear configuration in a material can be written as a Taylor expansion in fuction of nuclear positions. Or more specifically, of the deviation of nuclear positions from their equilibrium configuration.

$$\Phi = \Phi_0 + \sum_k \sum_i \Phi_i(k) u_i(k) + \frac{1}{2} \sum_{k,k'} \sum_{i,j} \Phi_{ij}(k,k') u_i(k) u_j(k') + \cdots \tag{2.2}$$

where $u_i(k)$ denotes the deviation of nucleus k in the Cartesian direction i from its equilibrium position $x_i^0(k)$. It is clear that

$$\Phi_i(k) = \left. \frac{\partial \Phi}{\partial x_i(k)} \right|_0, \quad \Phi_{ij}(k,k') = \left. \frac{\partial^2 \Phi}{\partial x_i(k) \partial x_j(k')} \right|_0 . \tag{2.3}$$

Since Φ_0 is assumed to be the equilibrium energy, $\Phi_i(k) = 0 \ \forall i,k$ and the expansion, in harmonic approximation, simplifies to

$$\Phi_{HO} = \Phi_0 + \frac{1}{2} \sum_{k,k'} \sum_{i,j} \Phi_{ij}(k,k') u_i(k) u_j(k'). \tag{2.4}$$

Relabeling k to $N\nu$, where N labels a unit cell, and ν labels a nucleus in the unit cell, the Hamiltonian in the harmonic approximation can be written as

$$\mathcal{H}_{HO} = \mathcal{T} + \frac{1}{2} \sum_{N\nu,M\mu} \sum_{i,j} \Phi_{ij}(N\nu, M\mu) u_i(N\nu) u_j(M\mu), \tag{2.5}$$

where $\mathcal{T}$ denotes the nuclear kinetic energy.

The dynamical matrix can be defined as

$$D_{ij}(\nu\mu, \mathbf{q}) = (m_\nu m_\mu)^{-\frac{1}{2}} N_0^{-1} \sum_{NM} \Phi_{ij}(N\nu, M\mu) \exp\{i\mathbf{q} \cdot [\mathbf{R}(N\nu) - \mathbf{R}(M\mu)]\}, \tag{2.6}$$

where $\mathbf{R}$ denotes a nuclear position vector, m denotes mass, N_0 refers to the number of nuclei considered and $\mathbf{q}$ is a wave vector.

Diagonalizing this dynamical matrix as a function of $\mathbf{q}$ yields the frequencies (and thus, energies) of the possible phonon vibrations with wavevector $\mathbf{q}$. With ξ the number of nuclei in a unit cell, there are 3ξ fundamental modes, called the phonon bands, for each $\mathbf{q}$. From these frequencies $\omega(\mathbf{q}, s)$, where s denotes the phonon band, one can determine dispersion relations, the density of states, and most importantly: the Helmholtz free energy. How this is done is explained in section 2.3.2.

The only material-dependent properties needed to calculate the dynamical matrix are the values of $\Phi_{ij}(N\nu, M\mu)$. Everything concerning phonons follows from these. In the finite displacement method, supercells are considered in which one nucleus is moved slighly from its equilibrium position, and the forces on all nuclei are determined. By displacing nucleus $M\mu$ by $\Delta x_j(M\mu)$, the corresponding column of the dynamical matrix can be calculated from

$$\Phi_{ij}(N\nu, M\mu) = \frac{\partial^2 \Phi}{\partial x_i(N\nu) \partial x_j(M\mu)} \approx -\frac{\partial}{\partial x_j(M\mu)} F_i(N\nu) \approx -\frac{F_i\left[N\nu; \Delta x_j(M\mu)\right]}{\Delta x_j(M\mu)}, \tag{2.7}$$

where $\Delta x_j(M\mu)$ is the displacement in the j-direction of nucleus μ in the primitive cell M.

$F_i\left[N\nu; \Delta x_j(M\mu)\right]$ is the i-component of the force on nucleus ν in the primitive cell N, caused by the displacement of nucleus $M\mu$ from its equilibrium position. This is shown graphically in fig. 2.1. When staying in the regime where the harmonic approximation is valid, the force should scale linearly with the displacement, and the values of the dynamical matrix should not depend on the specific value of $\Delta x_j(M\mu)$. The size of the supercell does matter, however. It should be large enough to include all positions on which the displacement of a single nucleus exerts a non-neglegible force.

If the primitive cell contains ξ nuclei, the dynamical matrix contains $(3\xi)^2$ values, which are almost never fully indepedent of each other. How many independent values there are depends on the symmetry of the material considered. For example, in the case of a non-magnetic monoatomic fcc material, one displacement is sufficient to determine $D_{ij}(\nu\mu, \mathbf{q})$ completely.

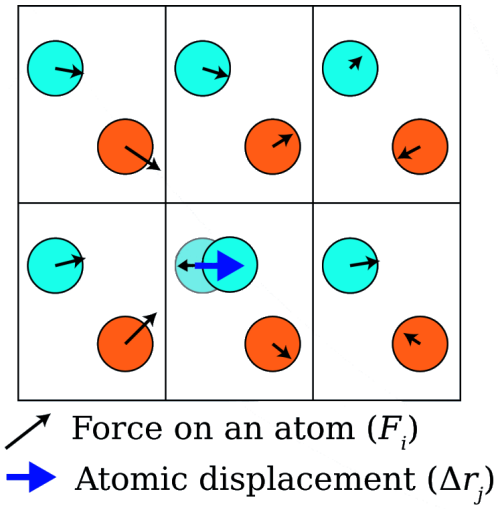

Figure 2.1: The relevant parameters in the finite displacement method for calculating the dynamical matrix

2.3.2 Thermodynamics with phonons

Raising the temperature of a material causes phonons to emerge in the lattice. These are intimitely related to the thermodynamic properties, which can be deduced through the machinery of statistical mechanics. Consider a discrete set of wavevectors $\{\mathbf{q}\}$, which constitutes a representative sampling of the first Brillouin zone. The partition function for this system, assuming all vibrational modes to be independent, is

$$Z = \prod_{\mathbf{q},s} Z_{\mathbf{q},s} = \prod_{\mathbf{q},s} \left(\sum_{n=0}^{\infty} \exp\left[-\frac{(\frac{1}{2}+n)\hbar\omega(\mathbf{q},s)}{k_B T} \right] \right) = \prod_{\mathbf{q},s} \frac{\exp\left(-\frac{1}{2}\frac{\hbar\omega(\mathbf{q},s)}{k_B T}\right)}{1-\exp\left(-\frac{\hbar\omega(\mathbf{q},s)}{k_B T}\right)}, \tag{2.8}$$

where $\omega(\mathbf{q}, s)$ denotes the frequency of the vibration mode with wave vector $\mathbf{q}$ in the s-th phonon band, and n is a dummy index used to count how many phonons are present for each vibrational mode.

This is directly related to the Helmholtz free energy F as $F = -k_B T \ln(Z)$.

$$F_{\text{discr}} = \frac{1}{2}\sum_{\mathbf{q},s} \hbar\omega(\mathbf{q},s) + k_B T \sum_{\mathbf{q},s} \ln\left[1 - \exp\left(-\hbar\omega(\mathbf{q},s)/k_B T\right)\right] \tag{2.9}$$

Note that the function above has been labeled as explicitly discrete, as equations (2.8) and (2.9) have been for an ensemble of discrete vibrational modes $(\mathbf{q}, s)$. Yet in an infinite solid, the reciprocal space is continuous, which means it is necessary to replace the sum over $\mathbf{q}$ with an integral. Going one step further however, this is a computational method, meaning discretization of the integral representation is necessary again to be able to calculate it

numerically. This can be summarized as follows:

$$\sum_{\mathbf{q},s} \xrightarrow{\infty \text{ solid}} \sum_{s} \int_{FBZ} d^3\mathbf{q} \xrightarrow{\text{Num. integration}} \frac{V_B}{N_\mathbf{q}} \sum_{\mathbf{q},s},$$

where $N_\mathbf{q}$ denotes the number of uniformly distributed $\mathbf{q}$-points used to sample the first Brillouin zone (FBZ) and V_B denotes the volume of the FBZ. This then yields the proper equation for numerically calculating the free energy F, from which the entropy S and heat capacity C_V follow as thermodynamic derivatives.

$$F = \frac{V_B}{N_\mathbf{q}} F_{\text{discr}} = \frac{V_B}{N_\mathbf{q}} \sum_{\mathbf{q},s} \frac{1}{2}\hbar\omega(\mathbf{q},s) + \frac{V_B}{N_\mathbf{q}} \sum_{\mathbf{q},s} k_B T \ln\left[1 - \exp\left(-\hbar\omega(\mathbf{q},s)/k_B T\right)\right] \quad (2.10a)$$

$$S = -\frac{\partial F}{\partial T} = -\frac{V_B}{N_\mathbf{q}} \sum_{\mathbf{q},s} k_B T \ln\left[1 - \exp\left(-\hbar\omega(\mathbf{q},s)/k_B T\right)\right] - \frac{V_B}{N_\mathbf{q}} \sum_{\mathbf{q},s} \frac{1}{T} \frac{\hbar\omega(\mathbf{q},s)}{\exp\left(\hbar\omega(\mathbf{q},s)/k_B T\right) - 1} \quad (2.10b)$$

$$C_V = T\frac{\partial S}{\partial T} = \frac{V_B}{N_\mathbf{q}} \sum_{\mathbf{q},s} k_B T \left[\frac{\hbar\omega(\mathbf{q},s)}{k_B T}\right]^2 \frac{\exp\left(-\hbar\omega(\mathbf{q},s)/k_B T\right)}{\left[\exp\left(-\hbar\omega(\mathbf{q},s)/k_B T\right) - 1\right]^2} \quad (2.10c)$$

Note that the constant factor $\frac{V_B}{N_\mathbf{q}}$ is necessary to make the expressions converge to finite values in the limit of $N_\mathbf{q} \to \infty$.

2.3.3 The quasi-harmonic approximation

The Helmholtz free energy does not suffice to fully describe a system under finite pressure. Also, a material in a purely harmonic picture does not expand as a function of temperature. To get a proper description of a material under both finite temperature and pressure, one should move to a formalism based on the Gibbs free energy G. Similar to the approach in 2.2, one can obtain the Gibbs free energy by determining the Helmholtz free energy as a function of volume. In the quasi-harmonic approximation, the volume is varied, and the Gibbs free energy is determined by

$$G(T,p) = \min_V \left[U(V) + F_{\text{lat}}(T,V) + pV\right]. \quad (2.11)$$

Where the pressure p is kept fixed, V is the primitive unit cell volume, U is the electronic energy contribution and F_{lat} is the free energy contribution from the harmonic lattice vibrations (phonons). F_{lat} is again calculated in the harmonic approximation, with the finite displacement method.

In practice, several values are chosen for the unit cell volume. Both the electronic energy and phonon properties are calculated for each of these values, after which an equation of state is fit for each considered temperature. From this fit, the Gibbs free energy can be deduced using equation (2.11). By repeating this process for several pressures, one can

determine a myriad of material properties as a function of both pressure and temperature.

The goal of this thesis is to do so for fcc iron at the conditions of the inner core of the planet Mercury. For example, using the above, it is possible to determine the density as a function of temperature and pressure, $\rho(T, p)$. Another possible parameter to calculate is the thermal expansion α,

$$\alpha(p, T) = \frac{V(p, T) - V(p, 0)}{TV(p, 0)}. \tag{2.12}$$

In the above, $V(p, T)$ denotes the volume at pressure p and temperature T, as determined through equation (2.11).

Chapter 3

Numerical convergence

When gathering scientific data, a careful assesment must be made of what level of accuracy is both necessary and obtainable. Every scientist loves higher accuracy, but an extra significant digit might not be worth spending time and effort on. On the other hand, how accurate is accurate enough? There are no generalamount answers to these questions, as much depends on what the data is needed for, and what resources are readily available. In computational science, the limiting resources are time and available computing power. Often, a decrease in accuracy can yield a decrease in calculation time, which means it can be useful to determine exactly what level of accuracy is needed in order to minimize calculation time. This section deals with the numerical convergence of VASP calculations, and with the level of convergence that can be achieved using particular accuracy settings. Mind that numerical convergence does not necessarily mean agreement with experimental values. There is much to say about this, which has already been covered in great detail elsewhere [27].

3.1 Convergence of structural properties in the ground state

In this section, VASP calculations will be considered of bulk fcc Fe at a temperature of 0 K and pressure of 0 Pa. VASP has several tunable parameters which allows a user to choose between accuracy and speed. (And hopefully, quite a bit of both.) The most relevant of these are EDIFF, the convergence criterion for the self-consistent field calculation; the number of k points for sampling the Brillouin zone; and ENCUT, the cut-off for the kinetic energy, defining how many plane wave basis states are used. To see what accuracies are achievable at what settings, the number of k points and the cut-off energy were varied independently, and several physical parameters (see below) were extracted from the data. For all calculations, EDIFF was set at 10^{-6} eV, and ISMEAR was set to the tetrahedron

method with Blöchl corrections.[1] Calculations were run as well with EDIFF at 10^{-4} eV, with neglegible differences in results. The k points were chosen with the Monkhorst-Pack scheme, choosing a grid of $n \times n \times n$ k points, where $n \in \{5, 7, 9, 11, 13, 17, 23, 29, 31, 33, 37\}$. Table 3.1 shows the corresponding number of irreducible k points. ENCUT was varied between 200 and 880 eV in steps of 40 eV. The corresponding number of plane wave basis set functions is also given in table 3.1.

Table 3.1: Number of irreducible k points in an fcc unit cell, using an $n \times n \times n$ Monkhorst-Pack scheme, and number of plane wave basis set functions used with an energy cutoff at ENCUT. For clarity, only the colored values are used in the figures below.

n	irr. k points	ENCUT	# of pl.w. func.
5	10	200	512
7	20	240	1000
9	35	280	1000
11	56	320	1000
13	84	360	1728
17	165	400	1728
23	364	440	1728
29	680	480	2744
31	816	520	2744
33	969	560	2744
37	1330	600	2744
		640	4096
		680	4096
		720	4096
		760	4096
		800	4096
		840	5832
		880	5832

For this test, the energy of the system was calculated at 23 distinct values for the unit cell volume between 9.1875 and 10.075 Å^3 using LDA [28], and between 9.85 and 10.85 Å^3 using GGA-PBE [29] [30], which corresponds to a range of about 9% around, but not centered on, the equilibrium volume. These values were fitted to a Birch-Murnaghan equation of state:

$$E(V) = E_0 + \frac{9V_0B_0}{16}\left\{\left[\left(\frac{V_0}{V}\right)^{\frac{2}{3}} - 1\right]^3 B_0' + \left[\left(\frac{V_0}{V}\right)^{\frac{2}{3}} - 1\right]^2 \left[6 - 4\left(\frac{V_0}{V}\right)^{\frac{2}{3}}\right]\right\}, \quad (3.1)$$

where V_0 is the equilibrium volume, E_0 is the equilibrium total energy, B is the bulk modulus and $B' = \frac{\partial B}{\partial P}$ is the derivitave of the bulk modulus.

[1] ISMEAR is a parameter VASP uses to simulate finite temperature of the electrons. Using no smearing would be unnatural for metals, as there is no bandgap. The tetrahedron method is a special way of weighted sampling of the Brillouin zone.

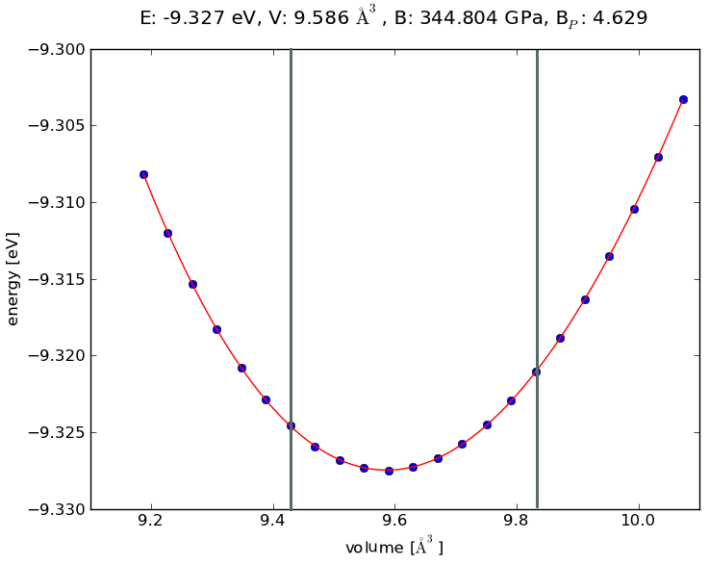

Figure 3.1: Fit through 23 data points for fcc Fe using LDA. 84 irreducible k points, cut-off energy of 400 eV. A decreased volume range is shown as well.

amount Figure 3.1 shows a fit through 23 points of the E(V) relation. The discrepancy between the fit and the data points is neglegible for all calculations run, as the total discrepancy was never more than around 5×10^{-4} eV for even the worst of fits, and most often not above 5×10^{-6} eV.

Figure 3.2 shows how much calculated values vary as a function of number of irreducible k points and size of the plane-wave basis set for LDA, using the results at the highest settings as reference. ΔE is the difference in energy between two arbitrary but fixed unit cell volumes. From the variational principle, it follows that the absolute total energy is always lower when taking a larger basis set. Therefor, only energies calculated at the same settings can be compared. In total, figure 3.2 is a summary of 1104 VASP calculations, 23 unit cell volumes for each combination of 8 k-point and 6 planewave settings. To pick an optimal setting for subsequent calculations, it is sufficient to look at the convergence of the most sensitive parameter, B'. By inspection, it is clear that taking 13^3 k points and an ENCUT of 480 eV yields well-convergenced results for B', and also for the other parameters. These same convergence tests were run using GGA-PBE, and similar results were obtained. The values found by picking both the highest number of k points ($37^3 \rightarrow 1330$ irreducible k points) and ENCUT (840 eV); and the "optimal" value of k points and ENCUT ($13^3 \rightarrow 84$, 480 eV) are shown in table 3.2. Also note that he value of ΔE itself has no real meaning and that only its convergenge is of importance.

The influence of the number of data points and range of considered volume was also considered. To decrease the volume range, points from the lower and upper end of the volume range (see Fig 3.1) were removed in pairs, leaving only the ones in the middle. To compare these effects with the effect of taking less data points, a number of data poins were

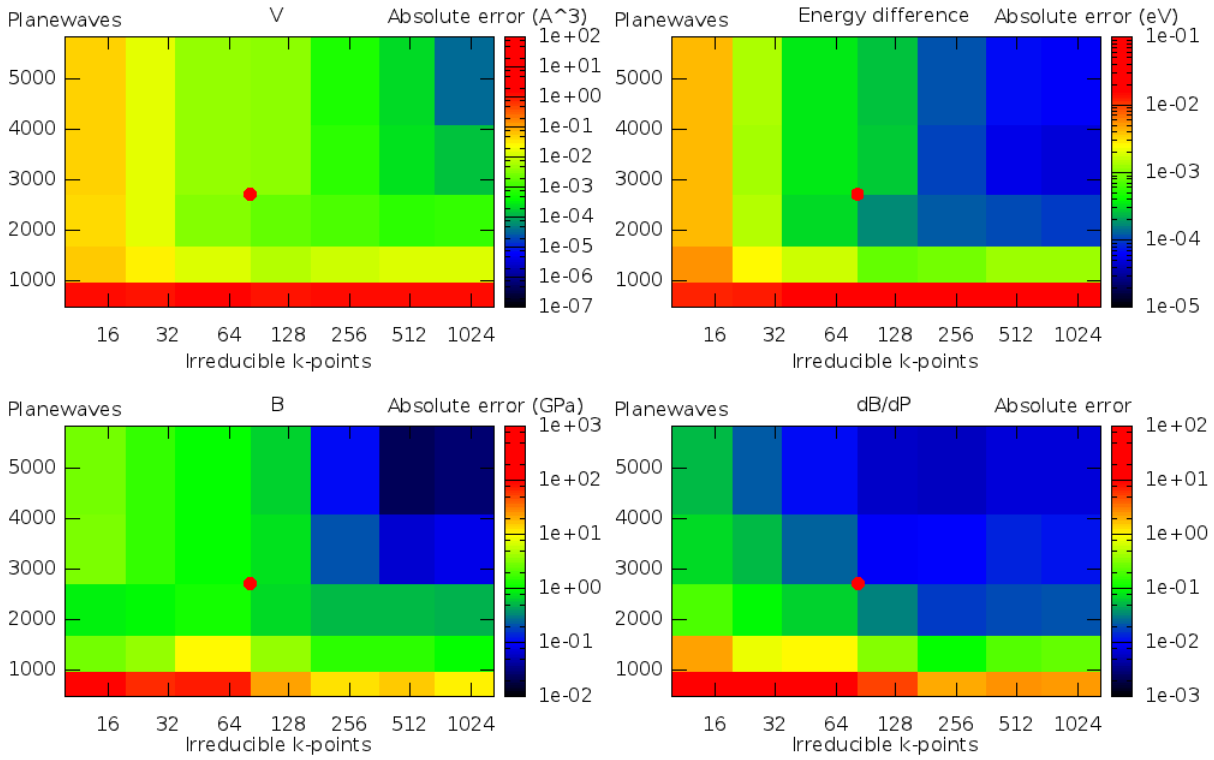

Figure 3.2: Discrepancy of parameters of fcc Fe calculated with LDA, compared to the values in table 3.2. The "optimal" point of 84 k points and ECUT = 480 eV is highlighted with a red dot.

removed as well in such a way to keep the range intact, and the sampling nearly uniform. The effects are shown in Fig 3.3 and Fig 3.4. The values for V_0 were almost completely unaffected, with deviations of less than 0.05% even when taking 5 or less data points at a severely limited range. For a reliable estimate of B and B′, 4 data points are an absolute minimum, as less points do not uniquely define a third order polynomial. From this data, it is clear that range is much more important than the number of points taken (note the scales of the axes). It is also clear that, again, B′ is the most sensitive parameter. Furthermore, higher accuracy can be seen to compensate for a limited volume range. Or in a more useful way, a larger volume range can compensate for taking a more limited basis set and sparser Brillouin zone sampling. Taking between 6 to 10 points over a range of about 10% around V_0 seems to be sufficient for a converged estimate of all considered parameters at the optimal settings. Do note however, that these ranges all contain the equilibrium volume. The effect of taking a volume range strictly above or below V_0 was not considered.

Table 3.2: Values of the equilibrium volume V_0, the equilibrium total energy E_0, an energy difference ΔE, the bulk modulus B, and the derivative of the bulk modulus $B' = \frac{\partial B}{\partial P}$ for fcc Fe at zero temperature and zero pressure. Calculated with LDA and GGA-PBE. "max" refers to calculations run with 1330 irreducible k points and a cut-off energy of 840 eV. "opt" refers to 83 irreducible k points, cut-off energy of 480 eV.

Parameter	LDA max	LDA opt	PBE max	PBE opt
V_0	9.5846 Å^3	9.5864 Å^3	10.2441 Å^3	10.2490 Å^3
E_0	-9.329723 eV	-9.327317 eV	-8.143407 eV	-8.140717 eV
ΔE	11.74 meV	11.89 meV	14.19 meV	13.78 meV
B	345.4 GPa	345.3 GPa	284.1 GPa	283.6 GPa
B′	4.583	4.578	4.674	4.656

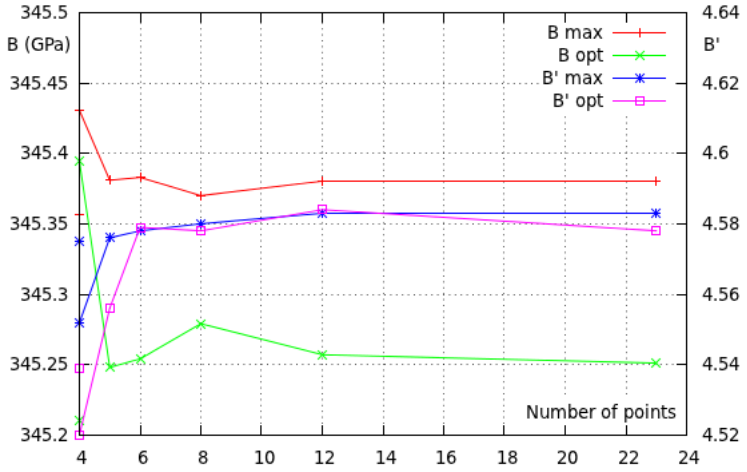

Figure 3.3: Values for bulk modulus B and its derivative B′ as a function of taking only n data points, but still spanning a volume range of about 9%, at both the optimal and maximal settings.

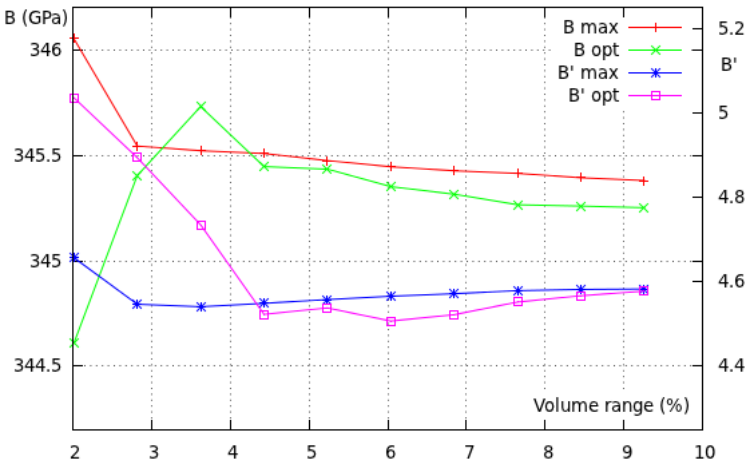

Figure 3.4: Values for bulk modulus B and its derivative B′ as a function of volume range, at both the optimal and maximal settings.

3.2 Convergence of forces

The accuracy of force calculations is highly important, since they form the basis for the calculation of phonon properties. As the symmetry of a pure fcc lattice would cause any displacement of the only atom in the unit cell to be a spatial translation of the full lattice, a larger, less symmetric unit cell must be considered. Fig. 3.5 and table 3.3 show the unit cell used for the calculations. The ions at Wyckoff positions 2a and 2c cannot have any force acting on them, as symmetry considerations forbid any net force. The force on each of these ions cancels out to zero in all calculations. The remaining nucleus at position 4f was displaced from its equilibrium position, so that there would be a net restoring force. This force was calculated to be 0.99937 eV/Å, a value which is fairly meaningless in itself, and serves only as an indication of the size of the force that was considered. The deviation from this value is shown in fig. 3.6. The number of irreducible k points shown in fig. 3.6 do not correspond to the values given in table 3.1, because of the different crystal symmetry. These values are given in table 3.4. As the number of plane waves is only influenced by the cut-off energy, those still correspond to the values in table 3.1.

Table 3.3: Crystal structure used to study the accuracy of calculated forces in Fe.

Symmetry space group	ITA nr.
$P6_3/mmc$	194
Basis vector	**Length (Å)**
a	3.7846
b	3.7846
c	6.6445
Cell angle	**Value**
α	90°
β	90°
γ	120°
Wyckoff positions	
2a	$(0, 0, 0)$
2c	$(1/3, 2/3, 1/4)$
4f	$(1/3, 2/3, 0.59338395)$

As can be seen in fig. 3.6, the settings from section 3.1 are sufficient here as well. There are two differences, however. To obtain properly converged values for the forces, a few modifications must be made to the VASP settings. One is the precision, which must be set as PREC = High to avoid so called wrap-around errors. The other is the EDIFF tag, which is best set to 10^{-8} eV to obtain accurate enough values for the forces.

To summarize, for this system of bulk fcc Fe at zero temperature and zero pressure, the settings which are sufficient for obtaining reliable results are shown in table 3.5.

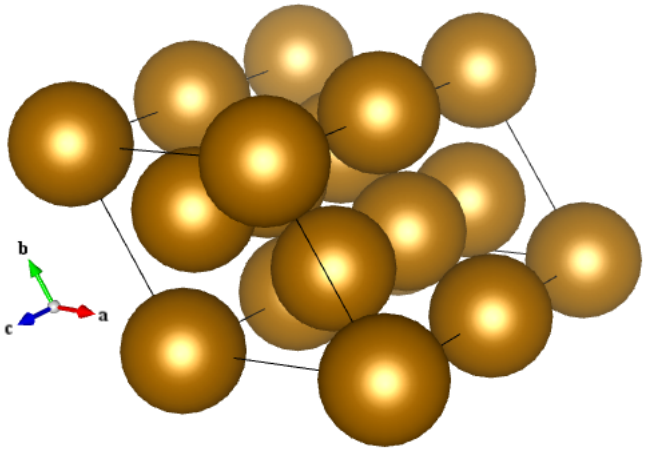

Figure 3.5: Crystal structure of the Fe unit cell used to test the convergence of force calculations. Details can be found in table 3.3

Table 3.4: Number of irreducible k points using the crystal structure of fig. 3.5 as unit cell, employing an $n \times n \times n$ Monkhorst-Pack scheme

n	irr. k points
5	15
7	32
9	60
11	96
13	147
17	297
23	672
29	1275

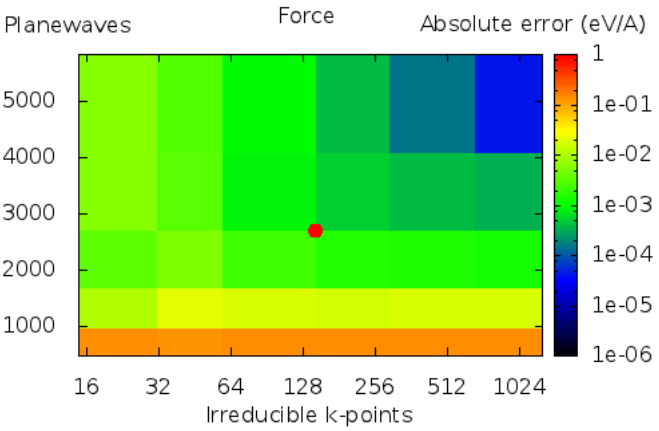

Figure 3.6: Deviation of the value for the force, as a function of the number of irreducible k points and number of plane waves in the basis set.

Table 3.5: Sufficient settings for obtaining reliable results for bulk fcc Fe at zero temperature and zero pressure using VASP, and what accuracy to expect for observable quantities. All are calculated with setting EDIFF $= 10^{-6}$, except the force calculations, which require EDIFF $= 10^{-8}$.

Setting	Value	Quantity	Accuracy
EDIFF	$10^{-6} - 10^{-8}$ eV	ΔE	0.5 meV
Irr. k points	84 (13^3)	E_0	5 meV
ECUT	480 eV	V_0	0.005 Å
Volume range	9%	B	0.2 GPa
Number of E(V) points	7	B′	0.01
		Forces	5 meV/Å

3.3 Convergence of thermal properties with respect to supercell size

The accuracy of the calculated thermal properties follows from an accurate description of the phonons which arise in the material. The accuracy of these phonon properties is determined by both the accuracy of the calculated forces, and the considered supercell size. The former was addressed in the previous section, the latter will be discussed now. There are several objects of which to consider the convergence: the phonon dispersion relations, the phonon density of states and the thermodynamic functions such as F, S and C_V.

As a first test, a $2 \times 2 \times 2$ supercell of fcc Pd was considered, and compared with data in ref. [27]. Using LDA and the lattice parameter as stated in ref. [27], the phonon dispersion was reproduced. This is shown in fig. 3.7. These dispersion relations, and all others in this section, will follow a path through reciprocal space consisting of three straight lines, Γ to X, X over U/K to Γ, and Γ to L. The labels of the high-symmetry points are shown in fig. 3.8.

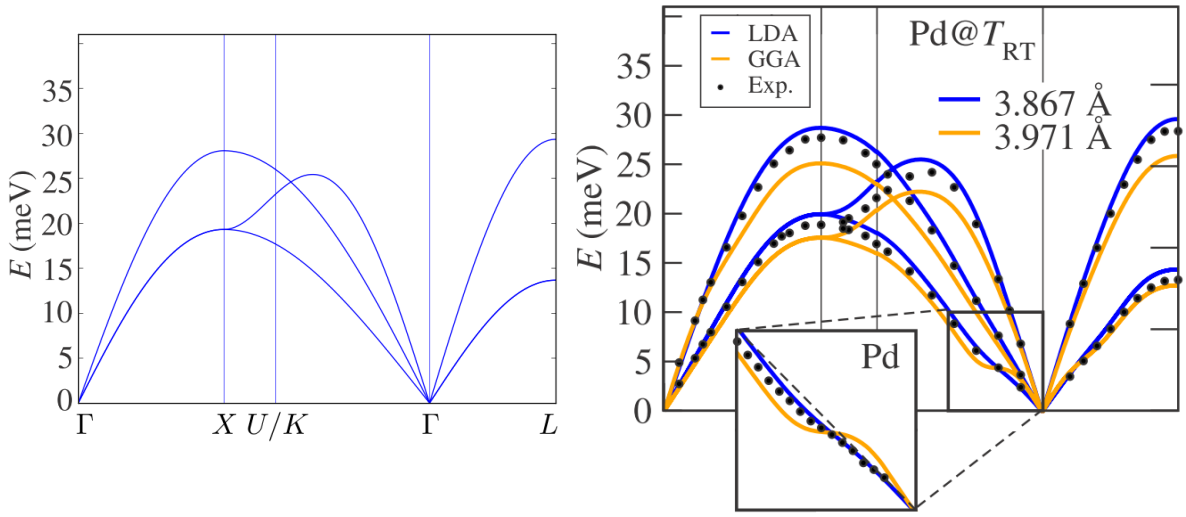

Figure 3.7: Phonon dispersion of fcc Pd. The figure on the left was calculated using a 2^3 supercell with the settings mentioned in table 3.5, using LDA and a lattice constant of 3.867 Å. The figure on the right was taken from ref. [27] for comparison, and was calculated using a 4^3 supercell size, emplying both LDA (blue) and PBE (yellow).

For our material of interest, fcc Fe, the phonon dispersion relations and phonon density of states were determined for supercell sizes of 2^3, 3^3, 4^3, 5^3 and 6^3, all calculations using a single displacement of a nucleus 0.01 Å from its equilibrium position. The result of this is shown in fig. 3.10.

Up to a supercell size of 3^3 these results show a good correspondence with literature, namely ref. [32], who used a 3^3 supercell. Higher up, however, the dispersion relations

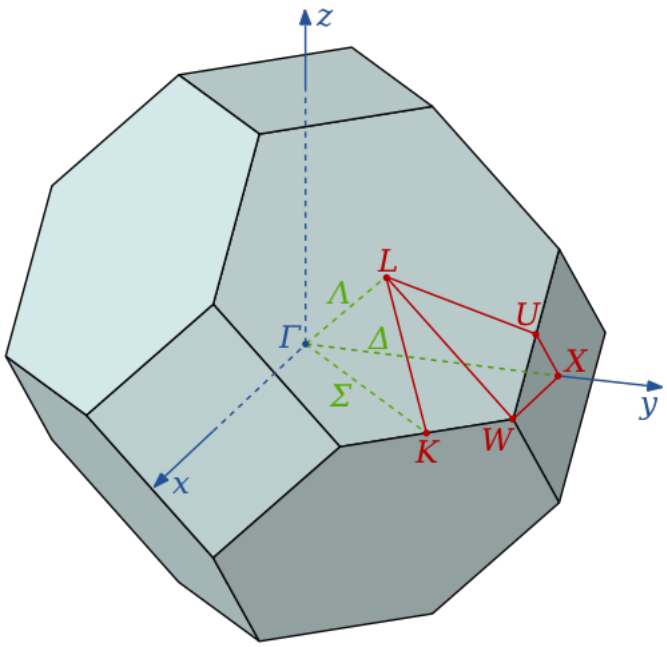

Figure 3.8: The surface of the first Brillouin zone of a face-centered cubic crystal lattice, with high-symmetry points marked. Note that K and U are equivalent.

begin to change. This is not due to long-range interactions, but is rather a limitation of the computational method to accurately determine forces. In all supercell sizes, VASP shows a spurious total drift force[2] of around 0.8 meV/Å. From a 4^3 supercell and up, the calculated long-range forces were all around this magnitude. The fact that forces of the same magnitude seem to appear at even larger distances at 5^3 and 6^3 supercell sizes gives a strong indication that these are not real forces, but artefacts resulting from the computational method. Furthermore, the sudden change in appearance of the dispersion curves, which looked a lot like other fcc dispersion curves before [27] (see fig. 3.7) indicates that these long-range forces are not real, but artefacts. Experimental data on fcc Fe [31] (see fig. 3.9) further confirms this. The real forces at these long ranges are almost certainly much lower than the accuracy which can be obtained using these methods.

Attempts have been made to increase the accuracy by increasing the number of k points in the Brillouin zone, by setting a more stringent energy convergence criterion EDIFF, and by increasing the displacement tenfold. This last option is useful since in the harmonic regime it should yield a tenfold increase in the forces. Despite this, the artificial dispersion relations remain.

It is clear that while larger supercells are needed to incorporate long-range interactions and their effect on the lattice vibrations, a too large supercell will overestimate these

[2]The total drift is the net force on the system itself, and is a measure of how accurate the force calculations in the system are. In an ideal case, these add up to zero due to obvious symmetry requirements. When they don't, every force comparable or smaller than this total drift force is suspicious and should not be taken at face value.

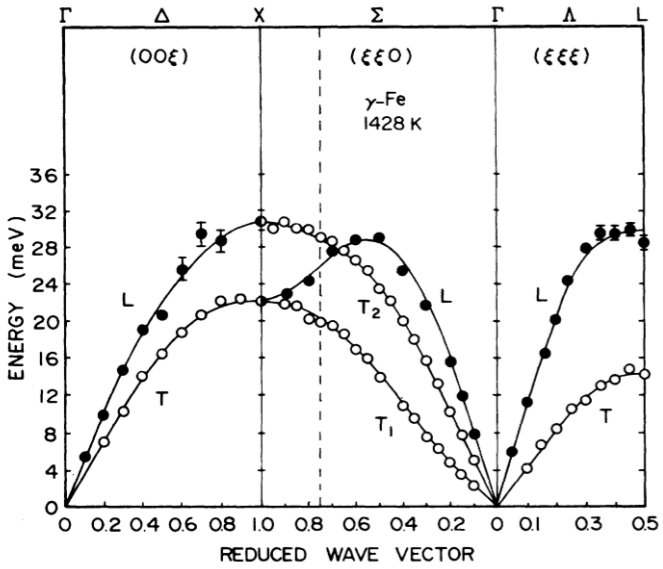

Figure 3.9: Phonon dispersion curves for fcc Fe taken experimentally by Zarestky and Stassis [31] at 1428 K and 0 Pa.

interactions due to computational artefacts. This is not a limitation however, as the artefacts only appear when the considered forces are so small that they become effectively neglegible. Since the forces are neglegible, a larger supercell is not needed, and a smaller supercell without artefacts suffices, circumventing the need to overcome what appears to be a fairly strong limit on accuracy.

The thermal properties were also calculated at various supercell sizes as described in subsection 2.3.2, this is shown in fig. 3.11. The force artefacts do not seem to have much effect on these thermal properties. This is because the thermodynamic functions arise from an integration over the entire Brillouin zone, such that small variations do not significantly contribute to the overall physical properties. Still, it is safer to use a 3^3 supercell, as it has no fictional long-range interactions.

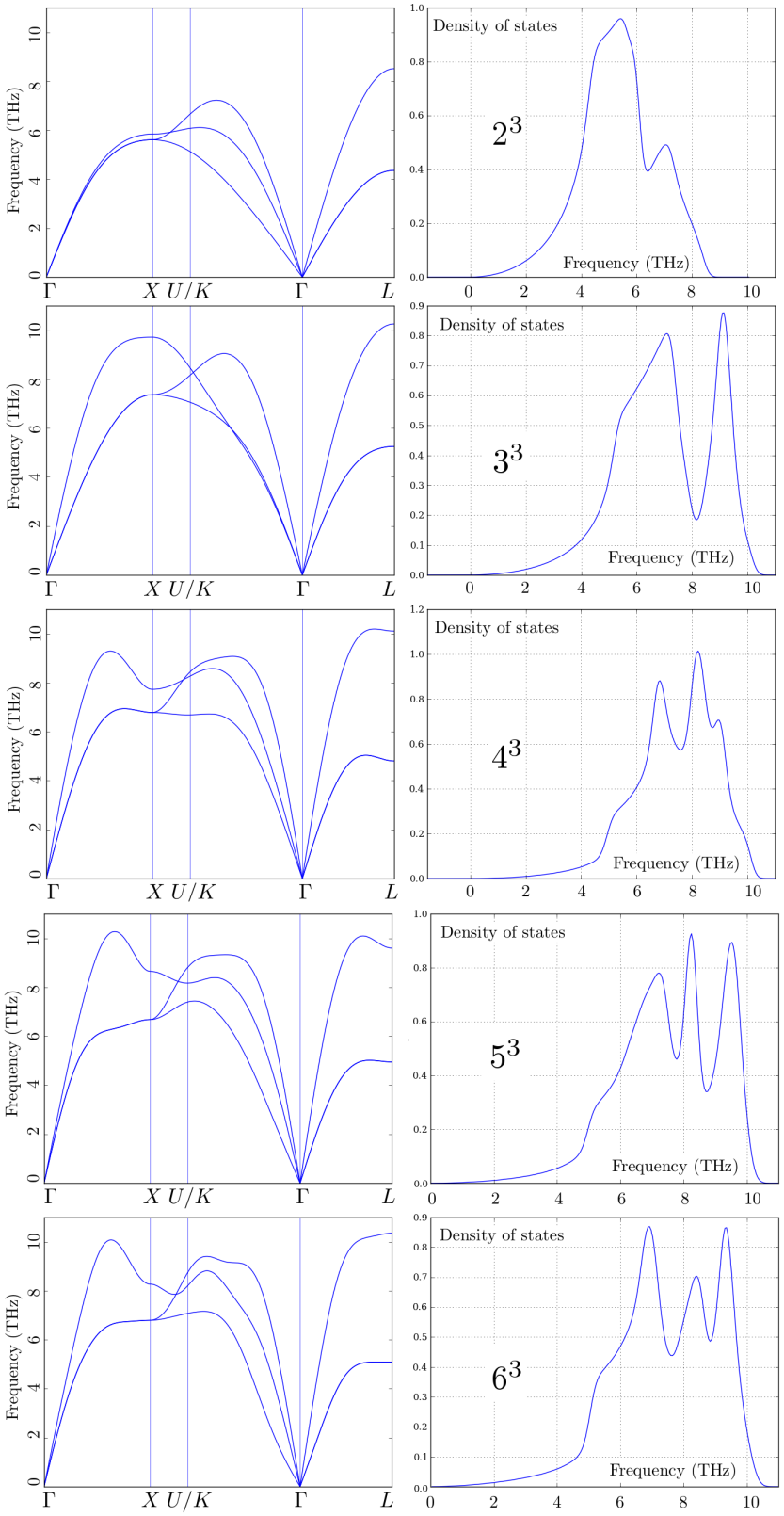

Figure 3.10: Phonon dispersion curves (left) and density of states (right) for non-magnetic fcc Fe in vacuum, calculated using (from top to bottom) a 2^3, 3^3, 4^3, 5^3, 6^3 supercell.

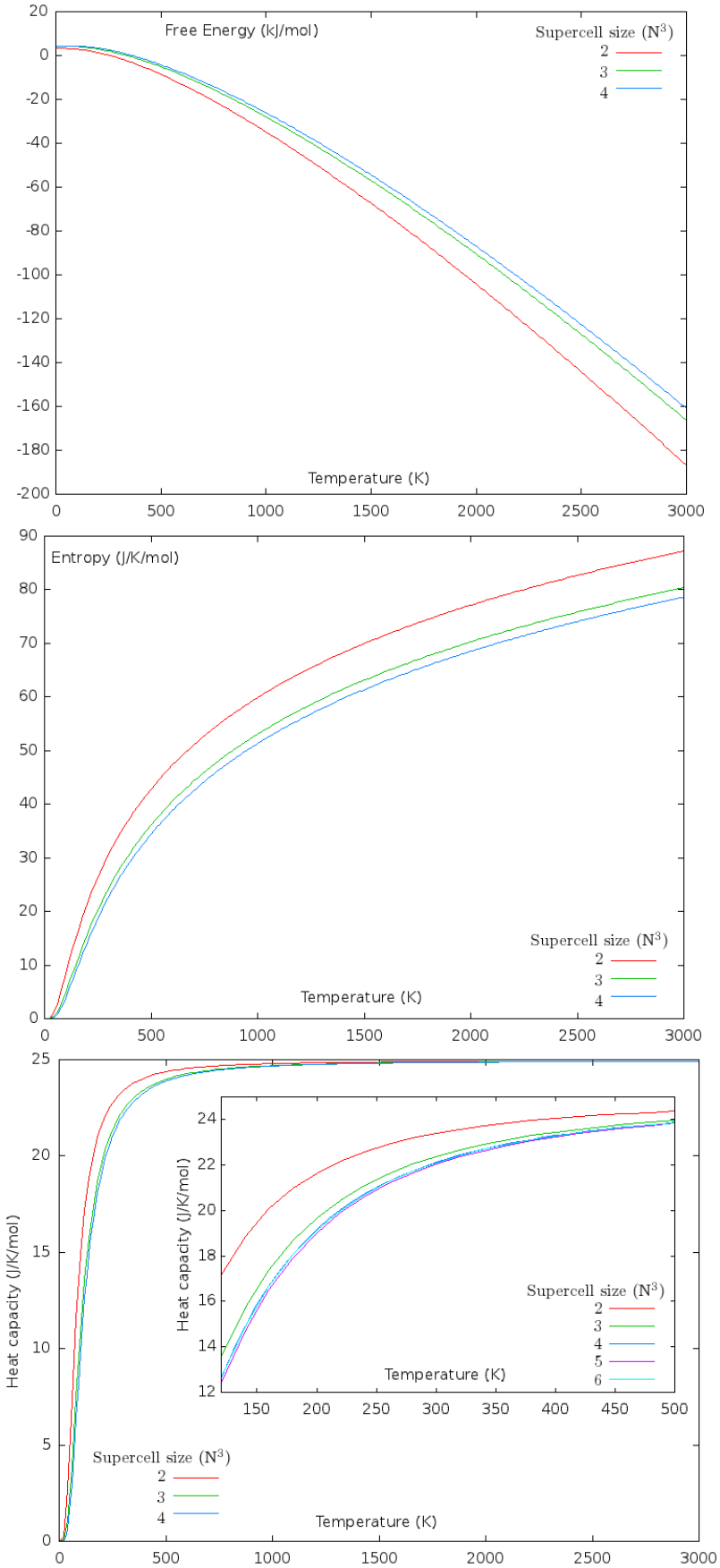

Figure 3.11: Helmholtz free energy, entropy and heat capacity for fcc Fe in vacuum, calculated with different supercell sizes.

Chapter 4

Results

The electronic energy and phonon properties of fcc Fe were calculated at 10 distinct values for the lattice parameter, using both LDA and PBE. The effect on the phonon dispersion relations by varying the lattice parameter is shown in fig. 4.1. Note that in this figure, the distance traveled from the first Γ point to the second Γ points decreases with increasing lattice parameter. This is the effect of the size of the reciprocal space being related to the size of the real space as

$$V_{\mathrm{FBZ}} \propto \frac{1}{V},$$

where V_{FBZ} is the volume of the first Brillouin zone. For this reason, there are no vertical lines drawn to denote the high-symmetry points, as they do not have the exact same position for every curve. Using the quasi-harmonic approximation (through equation 2.11), the Gibbs free energy was calculated at a large number of conditions for both temperature (0 to 3000 K) and pressure (0 to 100 GPa).

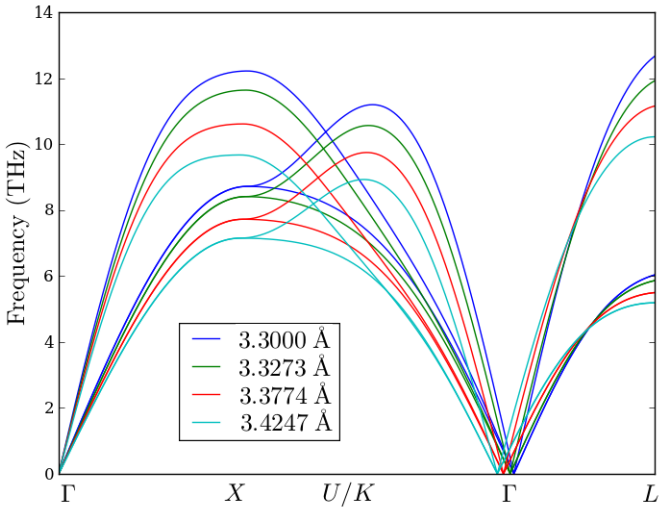

Figure 4.1: Phonon dispersion relations at four values of the lattice parameter, using LDA and a supercell of size 3^3. For comparison, the equilibrium lattice parameter at 0 K and 0 Pa is 3.3719 Å.

Fig. 4.2 shows a side-by-side comparison of phonon dispersion relations determined Zarestky and Stassis [31], and as calculated using the methods above. The chosen lattice parameter was 3.4969 Å , which is a value that was estimated based on the 0 K LDA equilibrium parameter (table 3.2) and a 0 Pa thermal expansion coefficient of $7.7 \times 10^{-5} K^{-1}$ [33].

$$V_{\mathrm{LDA}}(1428K) \approx V_{\mathrm{LDA}}(0K) + 1428K \times \alpha.$$

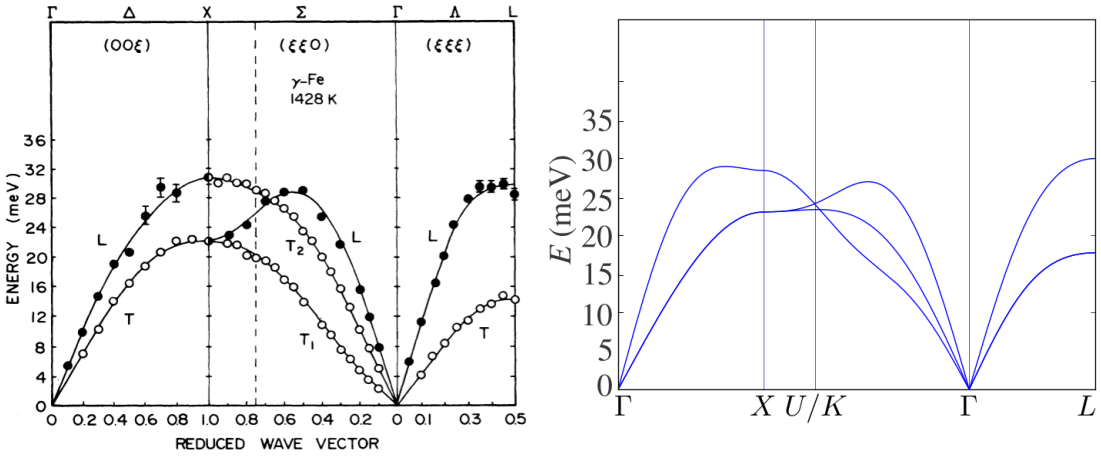

Figure 4.2: Phonon dispersion curves for fcc Fe taken experimentally by Zarestky and Stassis [31] (left) and calculated in this work (right). The experiment was done at a temperature of 1428 K and 0 Pa. The calculations were done employing LDA, using a 3^3 supercell with a lattice constant of 3.4969 Å.

To represent the results of the calculated volume of the primitive cell as a function of temperature and pressure, they are presented side-by-side with experimental data from Ahrens *et al* [34], Boehler *et al* [33] and Komabayashi *et al* [35] in table 4.1 and fig. 4.3.

Another parameter that was experimentally determined by Boehler *et al* was the thermal expansion of fcc Fe for pressures ranging from 4.5 to 16.8 GPa, and temperatures ranging from 1026 to 1919 K. The experimental data gave a range for the thermal expansion α of around $2 \times 10^{-5} K^{-1}$ to around $6 \times 10^{-5} K^{-1}$. The results of the calculations are shown in fig. 4.4. It must be remarked that Boehler *et al* use the volume at 300 K as reference volume, while in this work, the value at 0 K is used (equation 2.12). However, this should cause only a minor discrepancy.

Acet *et al* [36] determined the thermal expansion of fcc Fe experimentally between 1200 K and 1700 K without external pressure, finding it to be constant around the value of $2.33 \times 10^{-5} K^{-1}$. The calculated values for the thermal expansion in this work at these conditions were between $2.58 \times 10^{-5} K^{-1}$ and $2.73 \times 10^{-5} K^{-1}$.

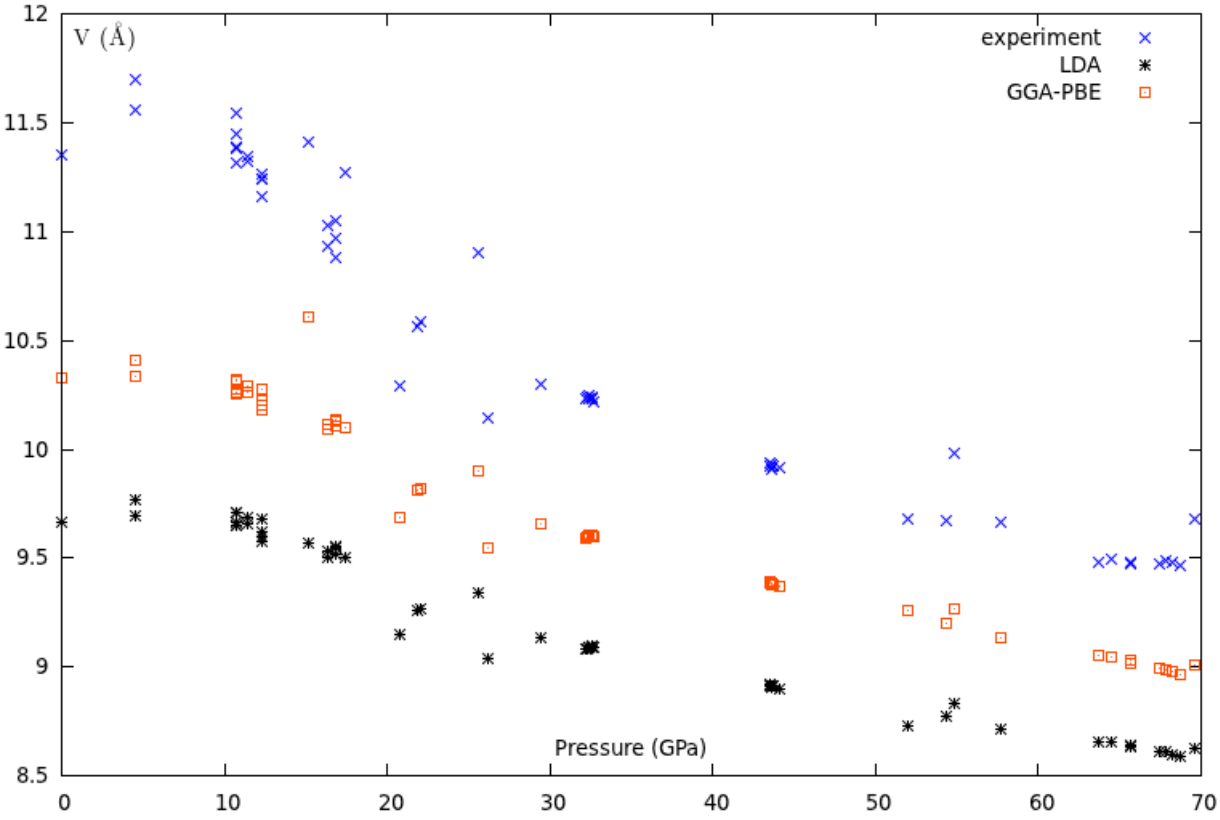

Figure 4.3: Visual representation of the data of table 4.1, showing how the volumes calculated with LDA and PBE compare to experimental data [34] [33]. Note that these are exerimental values taken at different temperatures (see table 4.1). For data points with equal pressure and unequal volume, the highest volumes correspond to the highest temperatures, both experimentally and computationally.

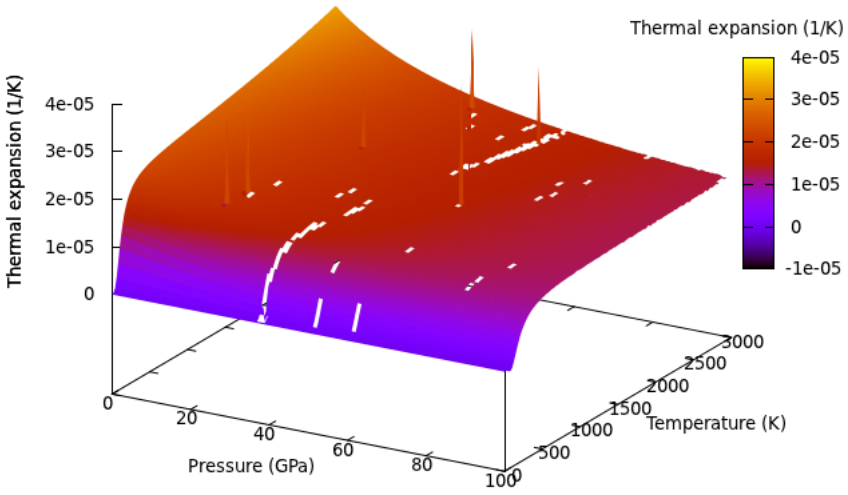

Figure 4.4: Thermal expansion as a function of temperature and pressure, calculated using LDA. White patches and spikes are numerical errors.

Table 4.1: Volumes V of the primitive cell of fcc Fe at various pressures P and temperatures T, as measured experimentally by Ahrens *et al* [34] (top), Boehler *et al* [33] (middle) and Komabayashi *et al* [35] (bottom). This is compared to the corresponding values which are determined computationally in this work, using LDA and PBE. This is also shown visually in fig. 4.3

P (GPa)	T (K)	V_{exp} (Å^3)	V_{LDA} (Å^3)	V_{PBE} (Å^3)
15.2	1848	11.41	9.57	10.61
17.4	1883	11.27	9.50	10.10
25.6	2012	10.90	9.34	9.90
54.8	2455	9.98	8.83	9.27
69.6	2767	9.68	8.627	9.01
0	300	11.350	9.662	10.331
4.5	1026	11.561	9.691	10.333
4.5	1364	11.695	9.770	10.410
10.7	1617	11.317	9.647	10.257
10.7	1645	11.381	9.652	10.261
10.7	1708	11.391	9.665	10.274
10.7	1870	11.446	9.706	10.313
10.7	1904	11.547	9.711	10.317
11.4	1756	11.345	9.659	10.264
11.4	1874	11.325	9.686	10.290
12.3	1505	11.159	9.577	10.180
12.3	1724	11.242	9.624	10.227
12.3	1595	11.242	9.598	10.201
12.3	1969	11.263	9.678	10.278
16.3	1657	10.930	9.504	10.090
16.3	1783	11.026	9.529	10.116
16.8	1965	10.968	9.553	10.138
16.8	1796	10.880	9.520	10.105
16.8	1919	11.048	9.545	10.130
22.1	1168	10.588	9.266	9.819
21.9	1093	10.567	9.260	9.812
20.8	300	10.289	9.148	9.686
29.4	1309	10.298	9.131	9.654
26.2	300	10.141	9.037	9.549
32.7	1443	10.221	9.087	9.598
32.6	1463	10.240	9.092	9.604
32.6	1478	10.233	9.095	9.608
32.4	1441	10.236	9.093	9.605
32.4	1411	10.249	9.089	9.601
32.3	1383	10.242	9.085	9.596
32.2	1354	10.236	9.082	9.593
44.1	1651	9.916	8.901	9.369
43.7	1677	9.925	8.912	9.381
43.5	1688	9.934	8.915	9.386
43.5	1695	9.925	8.918	9.389
43.6	1685	9.927	8.913	9.384
43.6	1648	9.907	8.907	9.377
54.4	1997	9.675	8.770	9.201
52.0	2017	9.679	8.732	9.256
57.7	2006	9.662	8.715	9.133
65.7	2318	9.473	8.630	9.019
67.4	2350	9.476	8.609	8.991
68.7	2359	9.467	8.589	8.966
68.2	2377	9.480	8.599	8.978
67.8	2409	9.485	8.608	8.989
65.7	2384	9.483	8.638	9.028
64.5	2360	9.492	8.654	9.049
63.7	2277	9.483	8.656	9.053

Chapter 5

Conclusion and outlook

It is possible to use *ab initio* methods to predict material properties of fcc iron as it probably exists at the core of the planet Mercury. From table 4.1 and fig. 4.3 it is clear that both LDA and PBE underestimate the unit cell volume. From fig. 4.4 and the comparison with experimental data in the previous section, one can see that the prediction for the thermal expansion using LDA corresponds to the value found by Acet *et al* [36].

From fig. 3.7 and fig. 4.2 it is clear that VASP/Phonopy are fairly accurate at predicting phonon dispersion relations, as long as the lattice parameter is chosen well. Fig. 4.1 shows clearly that the phonon frequencies are sensitive to changes in the lattice parameter. This means that care must be taken when comparing plots of dispersion relations, as unequal lattice parameters will lead to noticeable differences.

There are several possible ways to improve the quality of the calculated data. One way is to explicitly take anharmonic effects into account, especially since most of the experimental data was taken near the melting curve (see fig. 1.5). Although, by using the quasi-harmonic approximation, the anharmonic effect that phonon dispersion relations change with volume is already considered.

Another way is to study magnetic ordering effects and taking into account magnetic contributions to the entropy. Likewise, the electronic entropic contributions were neglected, and could be studied.

To summarize, future work on improving the data should focus on:

- Considering the effect of magnetic degrees of freedom, especially at lower pressure regimes.
- Considering electronic degrees of freedom, adding electronic contributions to the entropy.
- Taking into account anharmonic effects beyond the quasi-harmonic approximation.

From a planetological point of view, more work can be done to reliably predict the elastic coefficients of the material of the inner core, such as the bulk modulus, the shear modulus and Young's modulus. Also, since a planetary core does not consist of pure iron, there is much to study on the effects of alloying and the presence of impurities. A realistic core is an FeNi alloy, with S impurities [8]. The concentration of sulfur has a great influence on the size and state of Mercury's inner core [8], and computational methods could provide a way of correlating material properties of Mercury's core with the sulfur content.

Clearly, there are many ways in which ab initio methods can contribute to planetology.

To be continued...

Bibliography

[1] Martin Lara, Jess F. Palacin, Patricia Yanguas, and Carlos Corral. Analytical theory for spacecraft motion about Mercury. *Acta Astronautica*, 66(78):1022 – 1038, 2010.

[2] Robert G. Strom. Mercury - A post-Mariner 10 assessment. *Space Science Reviews*, 24:3–70, Sep 1979.

[3] Johannes Benkhoff, Jan van Casteren, Hajime Hayakawa, Masaki Fujimoto, Harri Laakso, Mauro Novara, Paolo Ferri, Helen R. Middleton, and Ruth Ziethe. BepiColombo - Comprehensive exploration of Mercury: Mission overview and science goals. *Planetary and Space Science*, 58(1-2):2 – 20, 2010.

[4] Tilman Spohn, Frank Sohl, Karin Wieczerkowski, and Vera Conzelmann. The interior structure of Mercury: what we know, what we expect from BepiColombo. *Planetary and Space Science*, 49(14-15):1561 – 1570, 2001.

[5] Helmut Harder and Gerald Schubert. Sulfur in Mercury's core? *Icarus*, 151(1):118 – 122, 2001.

[6] Sean C. Solomon. Mercury: the enigmatic innermost planet. *Earth and Planetary Science Letters*, 216(4):441 – 455, 2003.

[7] J. L. Margot, S. J. Peale, R. F. Jurgens, M. A. Slade, and I. V. Holin. Large longitude libration of mercury reveals a molten core. *Science*, 316(5825):710–714, 2007.

[8] A. Rivoldini, T. Van Hoolst, and O. Verhoeven. The interior structure of Mercury and its core sulfur content. *Icarus*, 201(1):12 – 30, 2009.

[9] M. Stampanoni, A. Vaterlaus, M. Aeschlimann, F. Meier, and D. Pescia. Magnetic properties of thin fcc iron films on Cu(001). *Journal of Applied Physics*, 64(10):5321 –5324, nov 1988.

[10] R. Boehler, A. Chopelas, and A. Zerr. Temperature and chemistry of the core-mantle boundary. *Chemical Geology*, 120(34):199 – 205, 1995.

[11] Wikipedia. Density functional theory — Wikipedia, The Free Encyclopedia, 2011. `http://en.wikipedia.org/w/index.php?title=Density_functional_theory&oldid=466377685` Online; accessed 23rd January 2012.

[12] Klaus Capelle. A bird's-eye view of density-functional theory. *Brazilian Journal of Physics*, 36:1318 – 1343, 12 2006.

[13] Richard M. Martin. *Electronic Structure: Basic Theory and Practical Methods*. Cambridge University Press, 2004.

[14] Reiner Dreizler Eberhard Gross. *Density Functional Theory*. Springer, 1995.

[15] P. Hohenberg and W. Kohn. Inhomogeneous electron gas. *Phys. Rev.*, 136:B864–B871, Nov 1964.

[16] W. Kohn and L. J. Sham. Self-consistent equations including exchange and correlation effects. *Phys. Rev.*, 140:A1133–A1138, Nov 1965.

[17] G. Kresse and J. Hafner. Ab initio molecular dynamics for liquid metals. *Phys. Rev. B*, 47:558, 1993.

[18] G. Kresse and J. Hafner. Ab initio molecular-dynamics simulation of the liquid-metal-amorphous-semiconductor transition in germanium. *Phys. Rev. B*, 49:14251, 1994.

[19] G. Kresse and J. Furthmller. Efficiency of ab-initio total energy calculations for metals and semiconductors using a plane-wave basis set. *Comput. Mat. Sci.*, 6:15, 1996.

[20] G. Kresse and J. Furthmller. Efficient iterative schemes for ab initio total-energy calculations using a plane-wave basis set. *Phys. Rev. B*, 54:11169, 1996.

[21] Warren E. Pickett. Pseudopotential methods in condensed matter applications. *Computer Physics Reports*, 9(3):115 – 197, 1989.

[22] C. Kittel. *Introduction to Solid State Physics*. Wiley, eighth edition, 2005.

[23] K. Huang M. Born. *Dynamical theory of crystal lattices*. The international series of monographs on physics. Oxford University Press, 1954.

[24] B. Grabowski, L. Ismer, T. Hickel, and J. Neugebauer. *Ab initio* up to the melting point: Anharmonicity and vacancies in aluminum. *Phys. Rev. B*, 79:134106, Apr 2009.

[25] A Togo, F Oba, and I Tanaka. First-principles calculations of the ferroelastic transition between rutile-type and CaCl2-type SiO2 at high pressures. *Phys. rev. B*, 78:134106, Oct 2008.

[26] K. Parlinski, Z. Q. Li, and Y. Kawazoe. First-principles determination of the soft mode in cubic ZrO_2. *Phys. Rev. Lett.*, 78:4063–4066, May 1997.

[27] Blazej Grabowski, Tilmann Hickel, and Jörg Neugebauer. *Ab initio* study of the thermodynamic properties of nonmagnetic elementary fcc metals: Exchange-correlation-related error bars and chemical trends. *Phys. Rev. B*, 76:024309, Jul 2007.

[28] J. P. Perdew and A. Zunger. Self-interaction correction to density-functional approximations for many-electron systems. *Phys. Rev. B*, 23:5048, 1981.

[29] J.P. Perdew, J.A. Chevary, S.H. Vosko, K.A. Jackson, M.R. Pederson, D.J. Singh, and C. Fiolhais. Atoms, molecules, solids, and surfaces: Applications of the generalized gradient approximation for exchange and correlation. *Phys. Rev. B*, 46:6671, 1992.

[30] J.P. Perdew, J.A. Chevary, S.H. Vosko, K.A. Jackson, M.R. Pederson, D.J. Singh, and C. Fiolhais. Erratum: Atoms, molecules, solids, and surfaces: Applications of the generalized gradient approximation for exchange and correlation. *Phys. Rev. B*, 48:4978, 1993.

[31] J. Zarestky and C. Stassis. Lattice dynamics of γ -Fe. *Phys. Rev. B*, 35:4500–4502, Mar 1987.

[32] Wenxu Zhang. Phonon softening by magnetic moment in γ-Fe. *Journal of Magnetism and Magnetic Materials*, 323(16):2206 – 2209, 2011.

[33] Boehler R., N. von Bargen, and A. Chopelas. Melting, thermal expansion, and phase transitions of iron at high pressures. *J. Geophys. Res.*, 95(B13):731736, May 1990.

[34] Ahrens T. J., K. G. Holland, and G. Q. Chen. Phase diagram of iron, revised-core temperatures. *Geophys. Res. Lett.*, 29(7):1150, Apr 2002.

[35] Komabayashi T. and Y. Fei. Internally consistent thermodynamic database for iron to the Earth's core conditions. *J. Geophys. Res.*, 115, Mar 2010. B03202.

[36] M. Acet, H. Zähres, E. F. Wassermann, and W. Pepperhoff. High-temperature moment-volume instability and anti-Invar of γ-Fe. *Phys. Rev. B*, 49:6012–6017, Mar 1994.